Electron Spin Resonance Investigations on the Location and Reducibility of Zirconium in Mesoporous Zr−MCM-41 Molecular Sieves

Karuna Chaudhari, Rajaram Bal, Tapan Kr. Das, Asha Chandwadkar, D. Srinivas, and S. Sivasanker*

Catalysis Division, National Chemical Laboratory, Pune 411 008, India

Received: June 5, 2000; In Final Form: September 6, 2000

Zirconium containing mesoporous MCM-41 molecular sieves with Si/Zr ratios of 96 (A), 55 (B), 39 (C), and 23 (D) were synthesized and characterized by X-ray diffraction (XRD), surface area and pore size distribution measurements, and FTIR, diffuse reflectance UV−visible (DRUV−vis), ^{29}Si MAS NMR, and electron spin resonance (ESR) spectroscopic techniques. The XRD patterns indicated an increase in the d_{100} spacing (from 36.77 to 40.88 Å) with increasing Zr content. The samples showed a characteristic oxygen to zirconium charge-transfer band at 210 nm in the DRUV−vis spectra, consistent with monatomic dispersion of zirconium in Zr−MCM-41. Reduction of zirconium from the +4 to the +3 state was achieved by reaction with $LiAlH_4$ at 298 K or with dry hydrogen at high temperatures. In samples A and B, Zr is located mostly in the pore walls, in substitutional locations (type I′) and in C and D, it is present at the surface of the pores (type I″) in addition to the substitutional locations. Zr(III) ions, in type I′ locations ($g_1 = 1.876$, $g_2 = 1.943$ and $g_3 = 1.970$), were resistant to reoxidation while those in type I″ locations ($g_{\|} = 1.899$ and $g_{\perp} = 1.961$) readily oxidized and formed $Zr^{IV}(O_2^{\bullet-})$ species. Interaction with H_2O_2 or γ-ray irradiation also produced the superoxo radical species. Irradiation resulted in two types of superoxo radical species, type II′ ions associated with surface Zr centers ($g_1 = 2.0319$, $g_2 = 2.0093$, and $g_3 = 2.0024$) and type II″ ions associated with defect centers ($g_1 = 2.0131$, $g_2 = 2.0098$, and $g_3 = 2.0045$). The ESR results of Zr(III) ions are compared with those of the isoelectronic Ti(III) centers in silicalite structures.

Introduction

Zirconia catalysts have wide applications,[1,2] though their industrial use as catalysts is limited partly by their low surface areas. Isomorphous substitution of Si by Zr in zeolites of the MFI and MEL structure types[3−5] results in the formation of microporous materials with catalytic activities similar to titanium containing molecular sieves. Zirconium substituted $AlPO_4$-5 (ZrAPO-5) has been reported to possess Brönsted and Lewis acidities and is active in the isomerization of *m*-xylene.[6] To preserve the remarkable catalytic properties of the zeolites while expanding their use to process bulkier molecules, a novel family of mesoporous M41S materials has been synthesized.[7−9] These all-silica materials become useful catalysts on substitution of elements such as Al,[10,11] Ti,[12−15] V,[16] and Sn.[17] Recently, the synthesis of zirconium containing mesoporous silica (Zr−MS/Zr−HMS) was reported using a primary amine (hexadecylamine) surfactant at room temperature.[18,19] These samples showed interesting properties as catalysts in the liquid-phase oxidation of organic molecules with alkyl peroxides. Occelli et al.[20] have reported the synthesis of isomorphously substituted Zr−MCM-41 and characterized the acidity by microcalorimetry experiments. However, the site geometry, coordination, and distribution of the Zr in the framework have not been established. In this work, we report the synthesis and characterization of isomorphously substituted Zr ions in MCM-41 and identify the nature and location of the Zr ions by ESR spectroscopic measurements after reduction of the Zr(IV) to Zr(III) ions by different methods. As far as we are aware, this is the first detailed ESR study on the location and redox behavior of zirconium in a silicalite (MCM-41) structure.

* Author for correspondence. E-mail: siva@cata.ncl.res.in. Fax: 91-020-589-3761.

Experimental Section

Materials. Si−MCM-41 and Zr−MCM-41 were synthesized by hydrothermal methods, using fumed silica (99%, Sigma), tetramethylammonium silicate (TMA silicate; 10 wt % silica solution, $TMA/SiO_2 = 0.5$; SACHEM Inc.), and cetyltrimethylammonium chloride/hydroxide (CTMACl/OH; 17.9 wt % Cl and 6.7 wt % OH) prepared in the laboratory by partial exchange of CTMACl (25 wt % aqueous solution, Aldrich) over an ion-exchange resin, tetramethylammonium hydroxide (TMAOH; 99%, Aldrich) and Zr butoxide ($Zr(OC_4H_9)_4$; 80 wt % solution in 1-butanol, Aldrich).

Synthesis of Si−MCM-41. The molar composition of the synthesis gel in terms of oxides was as follows: SiO_2: 0.086 $(NH_4)_2O$: 0.089 $(CTMA)_2O$: 0.155 $(TMA)_2O$: 40 H_2O.

Ammonium hydroxide (1.8 g; 25% solution) diluted with water (12.5 g) was added to a solution of CTMACl/OH (16.7 g; 24.6% solution) with stirring. To this mixture, 2.08 g TMAOH dissolved in 12.5 g water was added followed by the addition of 13.6 g TMA silicate. The thick gel formed was stirred for 20 min. Then, fumed silica (3.1 g) was added slowly to the above gel under stirring and the mixture was stirred further for 1 h. The pH of the final gel was 11.5. The gel was then transferred to a stainless steel autoclave and heated in an air oven at 383 K for 4 days for crystallization. After crystallization, the product was filtered, washed with deionized water, and dried at 373 K for 5 h. The product was finally calcined at 823 K for 3 h in nitrogen and then for 6 h in air.

10.1021/jp002031m CCC: $19.00
Published on Web 11/03/2000

TABLE 1: Composition and Physicochemical Characteristics of Si−MCM-41 and Zr−MCM-41 Samples

sample	SiO_2/ZrO_2 (mole ratio) gel	product	XRD d_{100} (Å)	unit cell parameter (Å)	BET surface area[a] (m^2/g)	pore diameter[a] (Å)	benzene sorption capacity (mass%)	pore volume[a] (cm^3/g)
Si−MCM-41	—	—	36.77	42.5	975	27	56.1	0.63
Zr−MCM-41(A)	100	96	38.38	44.3	968	28	60.9	0.75
Zr−MCM-41(B)	50	55	39.76	45.9	942	30	61.6	0.90
Zr−MCM-41(C)	25	39	40.88	47.2	889	31	62.4	1.05
Zr−MCM-41(D)	12.5	23	33.69	38.9	766	25	54.6	0.51

[a] Calculated from N_2 adsorption isotherm at liquid nitrogen temperature.

Synthesis of Zr−MCM-41. The molar composition of the synthesis gel in terms of oxides was as follows: SiO_2: 0−0.08 ZrO_2: 0.089 $(CTMA)_2O$: 0.155 $(TMA)_2O$: 18 H_2O.

In a typical synthesis, 24.6% solution of CTMACl/OH (16.7 g) was taken in a polypropylene beaker and 2.08 g TMAOH dissolved in 10 g water and 13.6 g TMA silicate were added to it while stirring. The thick gel formed was stirred further for 15 min. Fumed silica (3.1 g) was then added slowly for about 10 min to the above mixture under stirring; the stirring was continued for 1 h after completion of addition. To this thick gel, the required amount of $Zr(OC_4H_9)_4$ (e.g., 0.71 g for Si/Zr = 50) in 5−6 g of 2-propanol was added and the gel mixture was stirred for a further 1 h. The pH of the final gel was maintained at 11.5. The mixture was then transferred to a stainless steel autoclave and heated at 383 K for 5 days. The solid material (Zr−MCM-41) was then filtered, washed with deionized water, and dried at 373 K in air. The product was then calcined at 823 K in flowing nitrogen (for 3 h) and in flowing air (for 6 h) to remove the organic material.

A total of four samples with different Zr inputs (designated as Zr−MCM-41 (A), Zr−MCM-41 (B), Zr−MCM-41 (C), and Zr−MCM-41 (D) at Si/Zr input ratios = 100, 50, 25, and 12.5, respectively) were prepared following the general synthesis procedure described above using different quantities of zirconium butoxide.

Synthesis of Zr Impregnated MCM-41. The samples of Zr impregnated MCM-41 (Si/Zr = 25) were prepared by adding a solution of 0.32 g of $Zr(OC_4H_9)_4$ in 5 g of 2-propanol to 1 g of dry Si−MCM-41. The mixture was heated to dryness while stirring. The samples were finally calcined at 573 K for 4 h.

Physical Measurements and Sample Treatments. The crystalline phase identification and phase purity of the as-synthesized and calcined samples were checked by XRD (Philips, Holland) using a Nickel filtered Cu Kα radiation, (λ = 1.5406 Å, 40 kV, 25 mA) over $2\theta = 1-10°$. The chemical compositions of the samples were determined by wavelength dispersive XRF spectrometer (Rigaku 3070 E) with the Rh target energized at 50 kV and 40 mA. For XRF measurements glass beads of standards and samples were prepared by a borate fusion technique.

The sorption capacities for benzene were measured using a McBain Baker balance and a glass vacuum unit (10^{-5} Torr). Prior to sorption measurements, about 200 mg of the sample was activated at 673 K under vacuum. The surface area and pore diameters were determined from N_2 adsorption isotherms (obtained with a Coulter 100 instrument), using Barret-Joyner-Halenda (BJH) model.[21]

The diffuse reflectance UV−visible spectra of the samples were obtained using a Shimadzu (Model UV-2101 PC) spectrophotometer. Fourier transform infrared (FTIR) spectra (400−1300 cm^{-1}) of the samples as KBr pellets were recorded on a Pye Unicam SP-300 spectrophotometer.

The FT-NMR spectroscopic studies were carried out using a Bruker MSL 300 spectrometer. For the MAS NMR studies, finely powdered samples were placed in 7.0 mm O. D. zirconia rotors and spun at a speed of 2.5−3.3 kHz. Tetraethyl orthosilicate (δ = 82.4 ppm from TMS) was used as the reference compound for ^{29}Si.

The ESR spectra of calcined Si−MCM-41 and Zr−MCM-41 samples were recorded on a Bruker EMX spectrometer operating at X-band frequency and 100 kHz field modulation. The samples were taken in specially designed Suprasil quartz tubes (4.5 mm O. D.) having a provision for evacuation and adsorption of gases. The measurements at 77 K were carried out using a quartz insert Dewar. Spectral manipulations and simulations were done using Bruker WINEPR and Simfonia software packages. Microwave frequency was calibrated using a frequency counter fitted in the microwave bridge (Bruker ER 041XG-D) and the magnetic field was calibrated by using a (Bruker ER 035M) NMR Gaussmeter.

For ESR studies, the samples were initially evacuated (10^{-5} Torr) and dehydrated by gradually raising the temperature from 298 to 673 K in about 4−5 h and then kept at the required temperature for a further period of 16 h. These dehydrated samples were then subjected to hydrogen reduction by treating with dry hydrogen (20 mL/min) at high temperatures (673, 773, and 873 K) for 6 h.

Chemical reductions were done under argon atomosphere by reacting the dehydrated samples with $LiAlH_4$ in anhydrous distilled THF, at 298 K, for 6 h. The mixtures containing Zr−MCM-41 were then transferred to 4.5 mm O. D. quartz ESR tubes taking sufficient care to prevent contact with atmospheric oxygen.

The activated samples of Zr−MCM-41 were sealed in glass vials and reduced by exposure to γ-radiation generated from a ^{60}Co source at 77 K (total dose = 1.38×10^4 Gray at a dose rate of 2×10^3 Gray/h).

Results

Sample Characterization. The chemical analyses of Si−MCM-41 and Zr−MCM-41(A−D) are given in Table 1. The zirconium contents in Zr−MCM-41 samples were found to be less than those introduced in the synthesis gel (Table 1). The difference was more marked in samples C and D having higher amounts of zirconium.

X-ray Diffraction. As-synthesized samples of Si−MCM-41 and Zr−MCM-41 exhibited a typical four peak pattern that matched well with that reported by others for MCM-41.[8,9] These four reflections were indexed based on a hexagonal unit cell ($a = 2d_{100}/\sqrt{3}$) as described by Beck et al.[9] All the XRD peaks were relatively sharper in the as-synthesized Si−MCM-41 compared to Zr−MCM-41 samples. Except for Zr−MCM-41 (D), the peaks for the rest of the samples shifted to higher d spacing values with increasing Zr contents and suggest an incorporation of Zr in the framework locations.[22] On calcination, the peaks shifted to larger 2θ values due to condensation of the internal Si−OH groups giving rise to a contraction of the unit

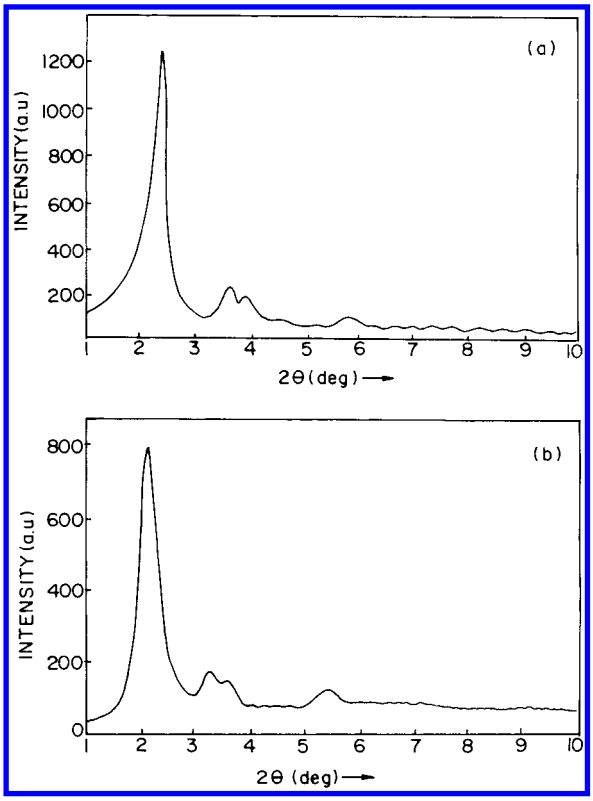

Figure 1. XRD patterns of calcined samples: (a) Si−MCM-41 and (b) Zr−MCM-41(C).

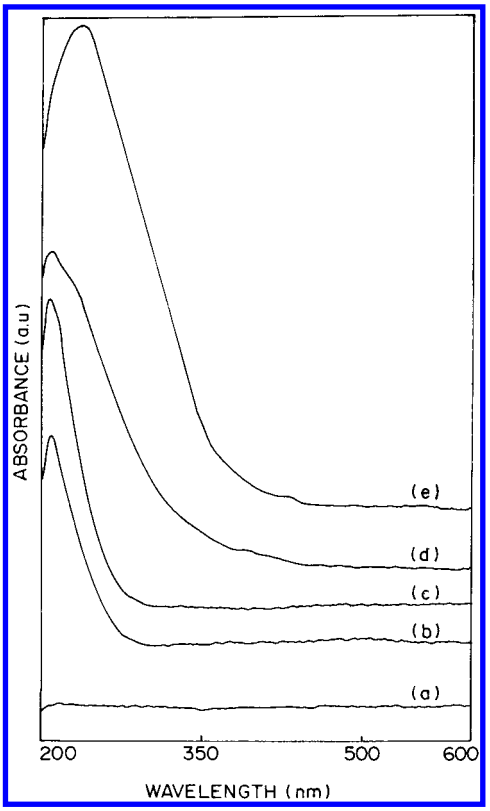

Figure 2. Diffuse reflectance UV−visible spectra of (a) Si−MCM-41, (b) Zr−MCM-41(B), (c) Zr−MCM-41(C), (d) Zr−MCM-41(D), and (e) ZrO_2.

cell.[9] The intensities of the peaks increased significantly in the calcined samples due to removal of the occluded surfactant molecules during the calcination process.[23] The XRD profiles of calcined Si−MCM-41 and Zr−MCM-41(C) samples are shown in Figure 1. The unit cell parameter (a_0) and d spacing for the calcined samples are listed in Table 1. The XRD patterns reveal that the long range order in hexagonal symmetry is retained in the calcined forms of both silicious and Zr containing MCM-41 samples.

Diffuse Reflectance UV−Visible Spectra. Figure 2 presents the UV−visible spectra of the calcined Zr−MCM-41 samples along with those of Si−MCM-41 and pure ZrO_2 samples. All the Zr containing samples exhibited a band around 210 nm attributable to an oxygen to Zr(IV) charge-transfer transition. This band in neat ZrO_2 occurred at 240 nm. A shift in the band position toward the higher energy side is attributed to the monatomic dispersion of zirconium in the Zr−MCM-41 samples. A similar shift in the charge-transfer band was observed earlier by others in Ti containing MCM-41 samples.[18,19] The broadening of the band with increasing Zr contents in the samples is probably because of the presence of more than one type of zirconium species. ESR studies of the reduced samples (vide infra) indeed support this observation.

Sorption Studies. The samples have been characterized further by N_2-sorption studies (Figure 3). The isotherms (type IV[24]) in general exhibited three stages of adsorption. The first stage ($p/p_0 < 0.2$) is due to a monolayer adsorption of nitrogen on the walls of the mesopores. The second stage, characterized by a steep increase in adsorption (p/p_0 between 0.25 and 0.45), is due to a capillary condensation inside the mesopores. This part shows hysteresis. The p/p_0 at which the inflection starts is related to the diameter of the mesopores. The sharpness in this step indicates a narrow pore size distribution.[25] The third stage in the adsorption isotherm is the near horizontal section beyond the p/p_0 of 0.35 due to a multilayer adsorption on the outer surface of the particles. In addition, a hysteresis loop at $p/p_0 > 0.8$ occurs due to capillary condensation in the interparticle mesoporosities.[24] As seen from Figure 3(b), the step of the isotherm shifts slightly toward higher p/p_0 with the incorporation of Zr indicating an increase in the pore size. The hysteresis loop broadened with an increase in the Zr content suggesting some disorder in the pore system arising from Zr incorporation. The BET surface area, pore diameter, and pore volume calculated by using the BJH model[21] are listed in Table 1. Incorporation of Zr in MCM-41 has a significant effect on these parameters. The pore diameter increased from 27 to 31 Å while the surface area decreased from 975 to 766 m^2/g with increasing Zr content.

FTIR Spectra. The framework IR spectra of the calcined Zr−MCM-41 samples revealed a band at 960 cm^{-1} attributable to polarized $SiO^{\delta-}\cdots Zr^{\delta+}$ bonds.[26] However, the silica MCM-41 samples also exhibited such a band at 960 cm^{-1} due to silanol groups at the defect sites. Hence, the presence of this band could not be used as evidence for the incorporation of Zr in the MCM-41 structure.[27]

^{29}Si MAS NMR Studies. The ^{29}Si MAS NMR spectra of Zr−MCM-41 samples did not differ significantly from those of Si−MCM-41 both in the as-synthesized and calcined forms. The samples exhibited broad resonance with chemical shifts at $\delta \approx -102$ and -112 ppm assigned, respectively to the Q^3 and Q^4 Si environments. Zirconium substitution did not yield any additional ^{29}Si peaks. The broadness of the ^{29}Si signals has been attributed to a large distribution of TOT angles.[9] As expected, due to dehydroxylation, the intensity of the Q^3 sites decreased on calcination of the samples.

ESR Studies. Calcined samples of Zr−MCM-41 were ESR silent both at 298 and 77 K. However, on evacuation (10^{-5} Torr; above 723 K for 5 h) a weak, isotropic signal centered at $g_{av} = 2.0023$ with a peak-to-peak line width of 6 G appeared. The intensity of the signal was proportional to the treatment

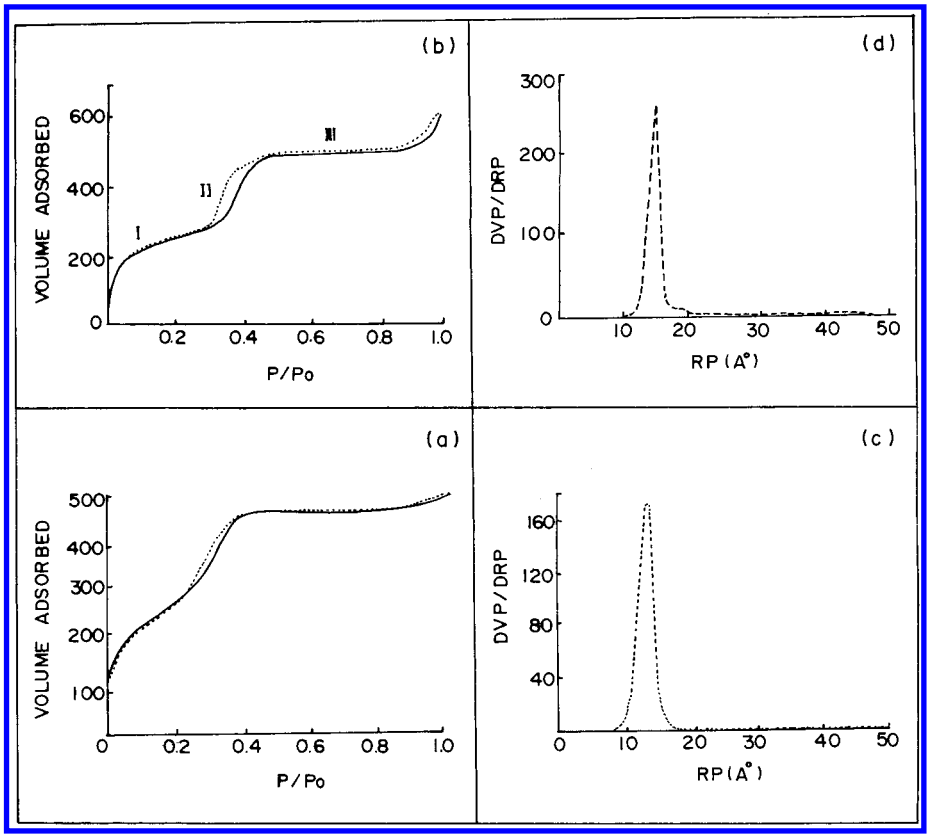

Figure 3. N_2 adsorption−desorption isotherms of (a) Si−MCM-41 and (b) Zr−MCM-41(C). Pore size distribution of (c) Si−MCM-41 and (d) Zr−MCM-41(C). I, II, and III represent the various stages of adsorption.

temperature. The spectrum became anisotropic ($g_{\|} = 2.0013$ and $g_{\perp} = 2.0028$) at higher temperatures (973 K). Representative ESR spectra of Zr−MCM-41(C), measured at 77 K, revealing the effect of thermoevacuation are shown in Figure 4. The origin of these signals is attributed to the presence of electrons trapped in oxygen vacancies (i.e., framework defects).

Zr−MCM-41 samples, after reduction with dry hydrogen at 673 K, exhibited spectra (at 77 K) corresponding two types of species, I and II. Species I is characteristic of a Zr(III) ion with $4d^1$ electronic configuration ($S = {}^1/_2$) and species II corresponds to a superoxide anion with a rhombic **g** symmetry ($g_1 = 2.0310$, $g_2 = 2.0076$, $g_3 = 2.0010$). Reduction experiments at different temperatures indicated that species I could be generated in high yields at 873 K. Si−MCM-41 samples after interaction with dry hydrogen did not show any ESR signal and hence, confirm the origin of species I and II as due to the heteroatom zirconium only. Despite our efforts, the interaction of Zr(III) ions (species I) with atmospheric oxygen could not be completely prevented. This interaction resulted in the formation of zirconium(IV) superoxide radical ions, $Zr^{IV}(O_2^{\bullet -})$ (species II). Figure 5 depicts ESR spectra, at 77 K, of Zr−MCM-41 samples with varying Si/Zr ratios. The signals and g values corresponding to species I and II are marked in the figure. The intensity of the signal due to species I increased with higher zirconium content.

Zr−MCM-41 samples could also be reduced by $LiAlH_4$. The 77 K ESR spectra of the reduced samples are shown in Figure 6. The spectra are similar to those of hydrogen reduced samples (Figure 5). It appears that Zr(IV) was reduced to a greater extent by $LiAlH_4$ than by dry hydrogen.

Zr(III) ions (species I) in samples Zr−MCM-41(C and D) were highly unstable toward molecular oxygen. Upon exposing the reduced samples to air, the signals due to species I decreased and those of species II ($Zr^{IV}(O_2^{\bullet -})$) increased. However, the behavior of species I in Zr−MCM-41(A) and Zr−MCM-41(B)

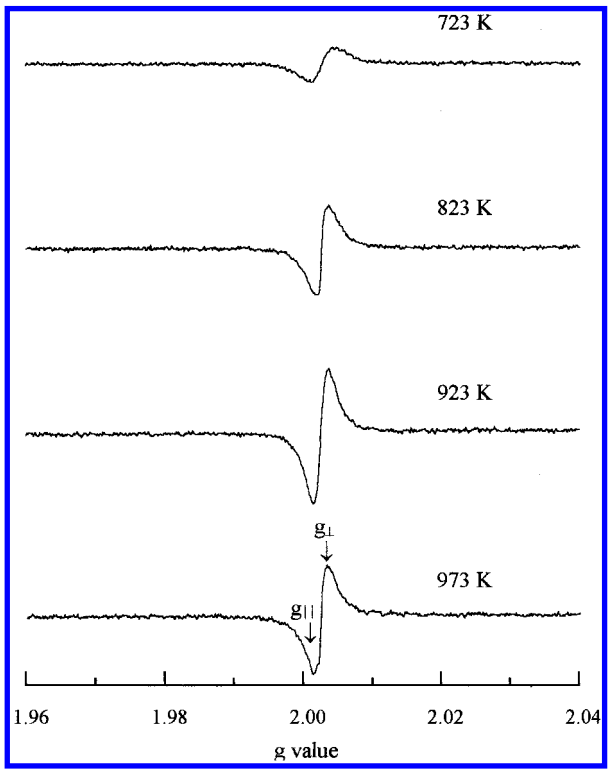

Figure 4. ESR spectra of Zr−MCM-41(C) after evacuation at different temperatures: MW freq. = 9.76 GHz, MW power = 2.52 mW, Receiver gain = 2.0×10^4, Modulation amplitude = 1 G, Time constant = 81.92 ms, Conversion time = 163.84 ms, Resolution in $X = 1024$, Number of scans = 5, and Temperature = 298 K.

was different. Species I in these samples was stable even after 16 h of contact with air. This observation therefore indicates the presence of at least two inequivalent Zr sites in Zr−MCM-

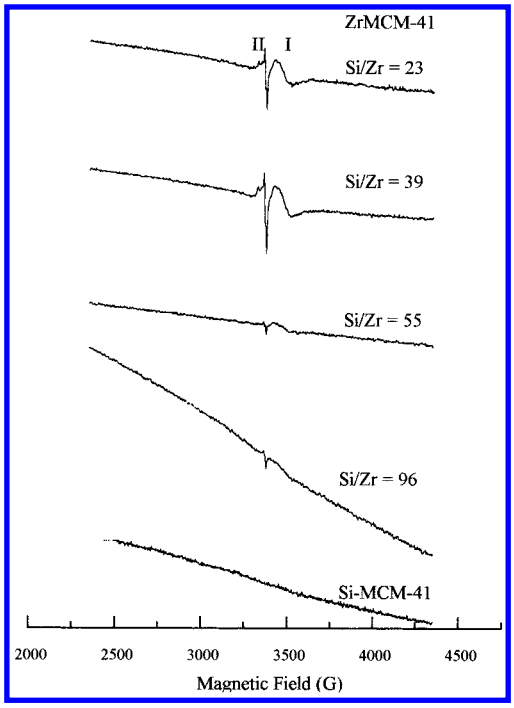

Figure 5. ESR spectra of Zr−MCM-41 samples after treatment with dry hydrogen. The *g*-values of signals corresponding to species I and II are marked. The broad background signal (for Si/Zr = 96) is due to dissolved oxygen in liquid nitrogen. MW freq. = 9.45 GHz, MW power = 3.98 mW, Receiver gain = 2.0×10^4, Modulation amplitude = 2 G, Time constant = 81.92 ms, Conversion time = 81.92 ms, Resolution in X = 1024, Number of scans = 3, and Temperature = 77 K.

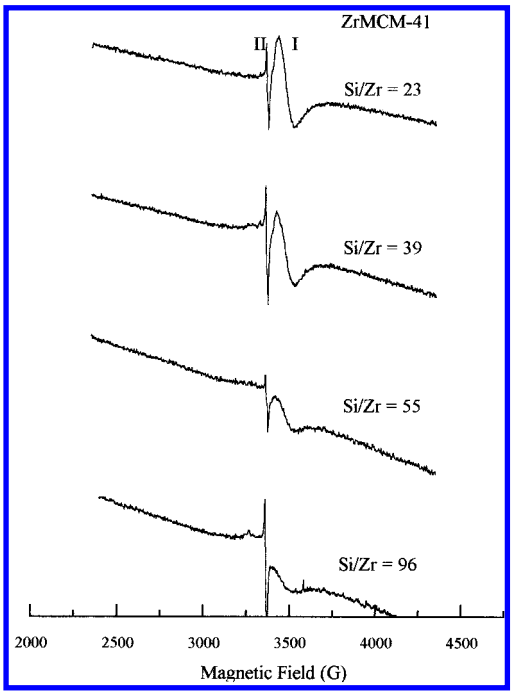

Figure 6. ESR spectra of Zr−MCM-41 samples with different Si/Zr ratios after reaction with $LiAlH_4$ in dry THF. MW freq. = 9.45 GHz, MW power = 3.17 mW, Receiver gain = 2.0×10^4, Modulation amplitude = 2 G, Time constant = 81.92 ms, Conversion time = 81.92 ms, Resolution in X = 1024, Number of scans = 3, and Temperature = 77 K.

41 samples. In samples containing lower amounts of zirconium Zr−MCM-41(A and B), the heteroatom is mostly incorporated in the framework structure of MCM-41, replacing the Si atoms. The substituted zirconum (probably in the walls) cannot be oxidized easily with molecular oxygen at 298 K. In contrast,

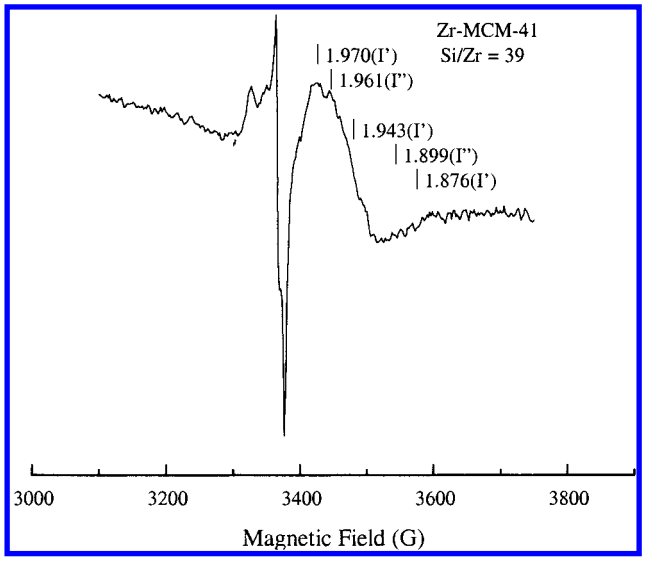

Figure 7. ESR spectra of Zr−MCM-41(C) after treatment with dry hydrogen. The signals corresponding to Zr(III) sites I′ and I″ are indicated.

the samples Zr−MCM-41(C and D) contain Zr both in substitutional locations (type I′) and at the surface of the pores (type I″). The latter type of Zr(III) ions (type I″), are highly reactive toward molecular oxygen and form $Zr^{IV}(O_2^{\bullet -})$ species (species II). The signals corresponding to types I′ and I″ are marked in Figure 7. The substitutional Zr(III) ions (type I′) are characterized by rhombic **g** values (g_1 = 1.876, g_2 = 1.943, and g_3 = 1.970) while the surface ions (type I″) are characterized by axial **g** values ($g_{||}$ = 1.899 and $g_{\perp}$ = 1.961).

Reduction of zirconium containing samples by γ-ray irradiation, at 77 K, yielded spectra typical of superoxide radicals (species II). Figure 8(b) shows the ESR spectrum for Zr−MCM-41(D) samples irradiated and measured at 77 K. Formation of two types of superoxide radicals (type II′ with g_1 = 2.0319, g_2 = 2.0093, and g_3 = 2.0024 and type II″ with g_1 = 2.0131, g_2 = 2.0098, and g_3 = 2.0045) are evident from Figure 8(b). Upon raising the temperature of the sample, species II″ almost disappeared and the spectrum (Figure 8(a)) corresponded mostly to species II′. Impregnated samples with the same Zr content showed a similar spectral pattern (Figure 8(c)) indicating that species II′ and II″ are due to two different types of surface superoxide anion radicals. As observed in the chemically reduced samples, even on γ-ray irradiation the Zr ions undergo reduction initially from the +4 to the +3 state. Subsequent oxidation of the Zr(III) ion due to interaction with atmospheric oxygen results in $Zr(O_2^{\bullet -})$ radical ions. The superoxide radical (species II′) could also be generated by interacting the Zr−MCM-41(C and D) samples with 50% H_2O_2 solution.

Table 2 lists the ESR spin Hamiltonian parameters of different species generated by chemical oxidation and γ-ray irradiation.

Discussion

The calcined Zr−MCM-41 samples showed ESR signals on thermoevacuation at $g_{||}$ = 2.0013 and $g_{\perp}$ = 2.0028. The origin of these signals could be attributed to the following reasons: (a) the presence of organic matter used as structure directing agents in the synthesis of MCM-41 samples, (b) hydrocarbons adsorbed from the vacuum system (vacuum grease or oil), and (c) F-centers (i.e., electrons trapped in the oxygen vacancies at the surface of the pores).

The presence of unburnt template molecules is ruled out as the samples were calcined at 823 K prior to the thermoevacu-

TABLE 2: ESR Spin Hamiltonian Parameters of Zirconium and Titanium Samples

system	treatment	g_1	g_2	g_3	assignment	reference
Zr−MCM-41	$H_2/LiAlH_4$	1.943	1.970	1.876	Zr(III); type I′	present work
		1.961	1.961	1.899	Zr(III); type I″	present work
		2.001	2.008	2.031	$Zr(O_2^{\bullet-})$; type II′	present work
Zr−MCM-41	γ-irr	2.0024	2.0093	2.0319	$Zr(O_2^{\bullet-})$; type II′	present work
		2.0045	2.0098	2.0131	superoxide species type II″	present work
zirconia/zirconia-hydroxide	Thermoevacuation	1.978	1.978	1.953	Zr(III)	29, 30
		2.0036	2.0096	2.0336	$Zr(O_2^{\bullet-})$	35−37
TS-1	CO/H_2	1.968	1.968	1.933	Ti(III)	31
Ti−MCM-41	γ-irr	1.967	1.967	1.901	Ti(III)	32
TiO_2 on porous Vycor glass	γ-irr	2.0036	2.0088	2.0268	$Ti(O_2^{\bullet-})$	35−37

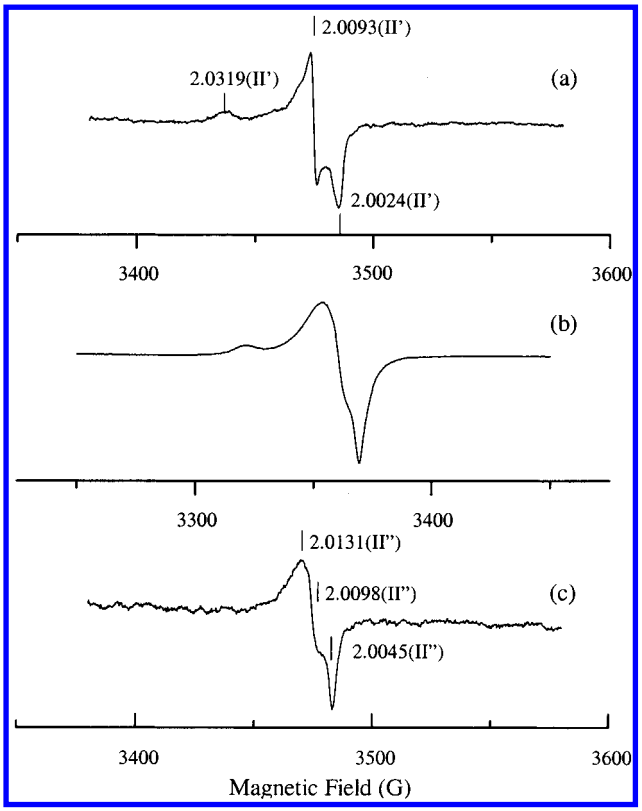

Figure 8. ESR spectra of γ-ray irradiated Zr−MCM-41(D) samples: (a) irradiated at 77 K, annealed, and measured at 298 K, (b) irradiated and measured at 77 K and (c) spectrum for the impregnated sample after irradiation at 77 K and measured at 298 K. The *g*-values of signals corresponding to species II′ and II″ are marked. MW power = 2.02 mW, Receiver gain = 2.0×10^4, Modulation amplitude = 2 G, Time constant = 81.92 ms, Conversion time = 163.84 ms, Resolution in *X* = 1024, Number of scans = 10. For (a) and (c) MW freq. = 9.77 GHz and for (b) MW freq. = 9.45 GHz.

ation studies. Also, necessary care was taken to prevent any adsorption of hydrocarbons from the vacuum system. Hence, the paramagnetic signals observed in the calcined Zr−MCM-41 samples on thermoevacuation are attributed solely to the F-centers. In support of this, we have also observed a change in the color of the samples from white to gray on thermal treatments. Formation of such defect centers was reported earlier on the surfaces of oxide materials,[28] zirconia,[29,30] and zirconium hydroxide-oxide.[30] However, in zirconia and zirconium hydroxide-oxide systems, Zr(III) ions ($g_{||} = 1.953$ and $g_{\perp} = 1.978$) were formed on thermal treatment, in addition to the defect centers.[28−30] However, in Zr−MCM-41, the thermal treatment did not result in Zr(III) ions. This is because of the difference in the redox behavior of zirconium in Zr−MCM-41 and neat zirconia samples. It also indicates the role of silica in stabilizing Zr(IV) ions.

The reduction of zirconium from the +4 to the +3 state was achieved by reactions with dry hydrogen or $LiAlH_4$. The XRD patterns revealed that the silicalite structure was unaffected during the reduction experiments with dry hydrogen at higher temperatures. ESR spectra are consistent with the presence of at least two different types of locations for zirconium: substitutional sites in pore walls (type I′) and isolated zirconium at the surface of the pores (either as substitution sites or as anchored/surface bound species (type I″)). In samples A and B, zirconium is isomorphously incorporated in the location of Si inside the pore walls while in samples C and D, it is present at the surface of the pores in addition to the substitutional sites inside the pore walls. Type I′ centers are characterized by a rhombic **g** tensor ($g_1 = 1.876$, $g_2 = 1.943$, $g_3 = 1.970$) and type I″ centers are characterized by an axial **g** tensor ($g_{||} = 1.899$ and $g_{\perp} = 1.961$). When a Zr(IV) ion having higher ionic radius (0.79 Å) occupies the Si location (ionic radius of Si = 0.41 Å), the local symmetry is distorted and hence, results in a rhombic **g** anisotropy. It is also interesting to note that the *g* values for Zr(III) ions (both type I′ and I″) in Zr−MCM-41 samples are different from those observed for pure zirconia samples ($g_{||} = 1.953$ and $g_{\perp} = 1.978$).[29,30] The deviation is mainly due to a change in the molecular symmetry. ESR and DRUV−vis spectra reveal the monatomic dispersion of surface zirconium ions. The spectroscopic techniques do not give any evidence for the presence of bulk zirconia in MCM-41. Hydrogen reduction experiments on impregnated samples (Si/Zr = 25) indicate that the intensity of the Zr(III) signal is about 10% lower in the case of Zr−MCM-41(A) compared to the impregnated samples indicating that a majority of the zirconium is at the surface of the pores while a small quantity is substituted for Si in the MCM-41 structure.

It is interesting to compare the spin Hamiltonian parameters of Zr(III) with Ti(III) in silicate molecular sieves. Both the ions are isoelectronic but the unpaired electron of Ti(III) occupies a 3d metal orbital while that of Zr(III) occupies a 4d orbital. Kevan et al.[31] have reported that Ti in titanosilicate molecular sieves TS-1 and titanium aluminophosphate molecular sieves (TAPO-5, TAPO-11, TAPO-31, and TAPO-36)[32] could be reduced by treating with CO or H_2. But Ti in an MCM-41 structure could not be reduced by H_2 even at 650 K, though reduction could be achieved by γ-irradiation.[33] Our observations suggest that Zr in MCM-41 could be reduced by H_2 at temperatures above 673 K. The signals for Ti(III) ions occurred at $g_{\perp} = 1.968$ and $g_{||} = 1.933$ in TS-1[31] and at $g_{\perp} = 1.967$ and $g_{||} = 1.901$ in γ-irradiated Ti−MCM-41 structures.[33] The deviation of *g* values (especially $g_{||}$) for Zr(III) from those of Ti(III) ions is worth noting. The energy level ordering of d orbitals in tetrahedral and octahedral crystal field environments is shown in Figure 9. In a tetrahedral crystal field, a d^1 ion has the ^2E state in the ground level. A further tetrahedral distortion removes the orbital degeneracy of the ground state as shown in Figure 9(a). If the distortion is positive (i.e., tetragonal compression), the $|0\rangle$ or

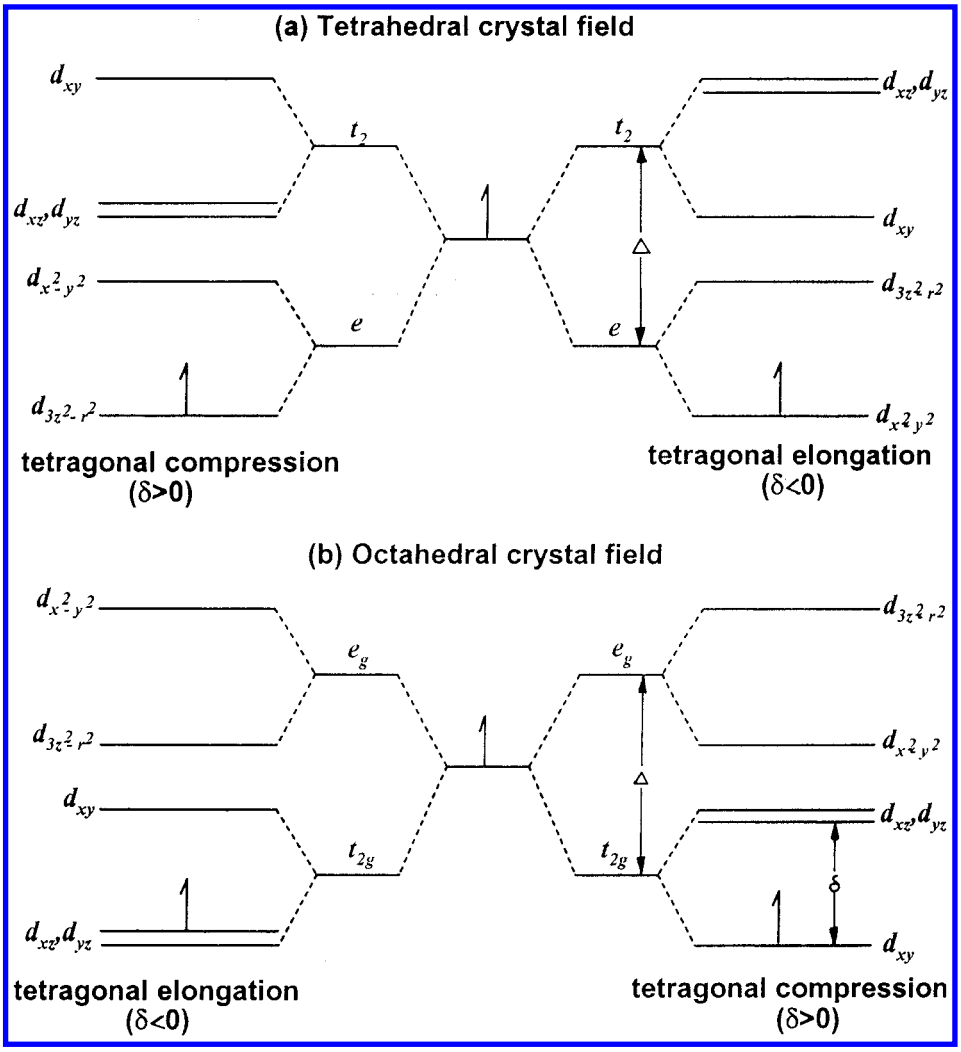

Figure 9. Energy level ordering of the metal d orbitals in (a) tetrahedral and (b) octahedral crystal symmetries.

$d_{3z^2-r^2}$ will lie lower in energy. Conversely, if the distortion is negative (i.e., tetragonal elongation), the $1/\sqrt{2}(|2\rangle + |-2\rangle)$ or $d_{x^2-y^2}$ state lies lower. Considering the distortion axis as the *z*-direction, the expressions for the *g* components, for an axial symmetry, at the first order are:

$$g_{\|} = 2.0023 \text{ and } g_{\perp} = 2.0023 - (6\lambda/\Delta)$$

for a positive distortion ($\delta > 0$) and

$$g_{\|} = 2.0023 - (8\lambda/\Delta) \text{ and } g_{\perp} = 2.0023 - (2\lambda/\Delta)$$

for a negative distortion ($\delta < 0$). In the former case ($\delta > 0$), $g_{\perp} < g_{\|} \approx 2.0023$ and in the latter ($\delta < 0$), $g_{\|} < g_{\perp} < 2.0023$, both the *g* components are smaller than 2.0023.

In an octahedral crystal field $^2T_{2g}$ is the ground state (Figure 9(b)). Thus, the ground state retains some orbital angular momentum even in the zero-order. An ESR signal is not observed for d^1 ions in purely octahedral symmetry. If the tetragonal distortion is positive, the spin doublet $1/\sqrt{2}(|2\rangle - |-2\rangle)$ or the d_{xy} orbital is the ground state and in such a case, the *g* components are expressed as follows:

$$g_{\|} = 2.0023 - (8\lambda/\Delta), g_{\perp} = 2.0023 - (2\lambda/\delta)$$

Hence, both the *g* values are predicted to be less than 2.0023 for d^1 ions in an octahedral crystal field with $0 < \delta \ll \lambda$ and $\Delta \gg \delta$. However, $g_{\perp}$ is larger than $g_{\|}$. The *g* values of Zr(III) in Zr−MCM-41 deviate very much from the free spin *g* value. The values with $g_{\perp} > g_{\|}$ for surface type I″ centers correspond to a distorted octahedral geometry while the *g* parameters with rhombic symmetry for type I′ centers are consistent with a distorted tetrahedral geometry. Low symmetry distortion for substitutional type I′ centers is probably due to the larger ionic radii of the guest Zr(IV) ion compared to the host Si(IV) ion. A smaller $g_{\|}$ value for Zr(III) compared to Ti(III) is due to the differences in the spin−orbit coupling constants of Zr (500 cm^{-1}) and Ti (155 cm^{-1}).[34]

The stability and location of Zr(III) centers (species I) were examined by exposing the reduced samples to atmospheric oxygen. The Zr(III) ions in samples A and B (having lower Zr content), were resistant to reoxidation at 298 K, even after 16 h of exposure to air. These centers in samples A and B are, therefore, attributed to the isomorphously substituted locations inside the pore walls of the MCM-41 structure (type I′). Conversely, samples C and D (having higher Zr content) were unstable and formed Zr(IV)-superoxide species soon after exposure to atmospheric oxygen. This reveals that Zr in samples C and D is mainly present at the surface of the pores (in extraframework or substitutional locations; type I″). The studies on samples containing various amounts of zirconium (Figure 5) indicate that zirconium at a level of 2 mol % can be substituted for Si in the framework structure of MCM-41. It is interesting to note that while the zirconium ions situated in the pore walls (type I′) could be reduced by hydrogen, they could

not be reoxidized by dioxygen at 298 K. These species are probably located in tetrahedral layers below the pore surface where the bulkier dioxygen does not have much access to reoxidize Zr(III) back to Zr(IV). In contrast, the zirconium species at or near the pore surface has a fair access for the interaction with molecular oxygen to form $Zr(O_2^{\bullet-})$ species.

Exposure of Zr−MCM-41 and Zr impregnated Si−MCM-41 samples to γ-radiation resulted in the formation of two types of superoxide species (type II′ and II″). Type II′ species with higher g anisotropy were unstable on annealing while type II″ species having lower g anisotropy were stable. The g parameters of type II′ are similar to the superoxide ion observed in the reduced samples. Hence it is proposed that Zr(IV) is initially reduced to Zr(III) by γ-radiolysis and that these surface Zr(III) centers on interaction with atmospheric oxygen result in $Zr(O_2^{\bullet-})$ anions. The interaction of aerial oxygen with defect centers can also generate superoxide ions. These are expected to have lower g anisotropy. Formation of such superoxide anions on the silica surface is well-known. The origin of type II″ species is associated with the defect sites. The superoxide ions formed upon irradiation of TiO_2 highly dispersed on porous Vycor glass showed signals at $g_1 = 2.0268$, $g_2 = 2.0088$, and $g_3 = 2.0036$. The superoxide ions at the surface of ZrO_2 are characterized by $g_1 = 2.0336$, $g_2 = 2.0096$, and $g_3 = 2.0036$.[36−38] The similarity in g components of type II′ species ($g_1 = 2.0319$, $g_2 = 2.0093$, and $g_3 = 2.0024$) and those on ZrO_2 reveals that these radical centers are associated with surface Zr(IV) ions. Type II″ species were not observed in hydrogen or $LiAlH_4$ reduced samples. The g_1 parameter of the superoxide anion is sensitive to the metal ion and its oxidation state it is bound to.[36] Assuming that the z direction corresponds to the internuclear axis and the y direction to the orbital hosting the unpaired electron, the expression for the g parameters of the superoxide anion at the first order in λ', Δ, and E are written as

$$g_1 = 2.0023 + 2\lambda'/\Delta$$

$$g_2 = 2.0023 + 2\lambda'/E$$

$$g_3 = 2.0023$$

Here λ' is the spin−orbit coupling constant for the oxygen atom and E and Δ are the energy separations between $2p\sigma$ and $2p\pi y^*$ and $2p\pi x^*$ and $2p\pi y^*$, respectively. Although the oxidation state of titanium and zirconium in the superoxide species is the same, the differences in the g values are attributed to a difference in the covalency parameter as well as the energy separation between $2p\pi x^*$ and $2p\pi y^*$ orbitals. Probably the Zr−O bond is less covalent than the Ti−O bond and hence results in a larger g_1 value for $Zr(O_2^{\bullet-})$ than for $Ti(O_2^{\bullet-})$ species. The probable locations of zirconium ions in mesoporous MCM-41 samples and the reduction mechanism are presented in Scheme 1.

Conclusions

Mesoporous zirconium containing MCM-41 samples with Si/Zr ratios of 96, 55, 39, and 23 were synthesized and characterized. The zirconium ions could be reduced by reacting with dry hydrogen, $LiAlH_4$, and γ-ray irradiation. ESR investigations reveal that zirconium is incorporated in place of Si in the pore walls of Zr−MCM-41 to a level of 2 mol %. Zirconium is mostly in the substitutional locations in samples with Si/Zr = 96 and 55. The samples with Si/Zr = 39 and 23 contain zirconium at the surface of the pores in addition to the zirconium located in the pore walls. The surface zirconium sites are highly reactive to oxygen and form zirconium(IV)-superoxide species.

SCHEME 1

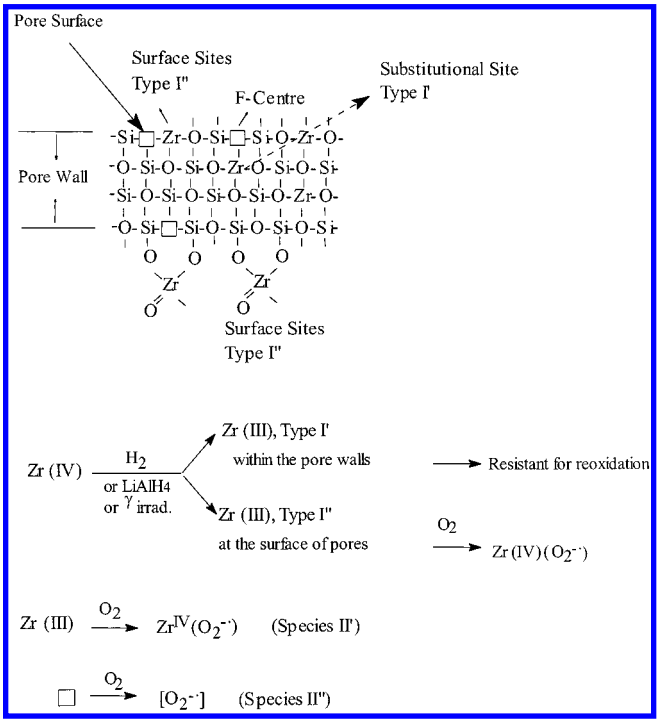

The facile redox behavior of Zr in MCM-41 is probably responsible for its reactivity in the liquid-phase oxidation of organic molecules with alkyl peroxides.

Acknowledgment. The authors thank Mr. S. Banerjee for help in reduction experiments. K.C. and R.B. acknowledge CSIR, New Delhi, for financial support in the form of Senior Research Fellowship.

References and Notes

(1) Tanabe, K.; Yamaguchi, T. *Catal. Today* **1994**, *20*, 185.
(2) Yamaguchi, T. *Catal. Today* **1994**, *20*, 199.
(3) Wang, G.; Wang, X.; Yu. S. *Stud. Surf. Sci. Catal*. **1993**, *83*, 67.
(4) Dongare, M. K.; Singh, P.; Moghe, P.; Ratnasamy, P. *Zeolites* **1991**, *11*, 690.
(5) Rakshe, B.; Ramaswamy, V.; Hegde, S. G.; Vetrivel, R.; Ramaswamy. A. V. *Catal. Lett.* **1997**, *45*, 41.
(6) Dongare, M. K.; Sabde, D. P.; Shaikh, R. A.; Kamble, K. R.; Hegde, S. G. *Catal. Today* **1999**, *49*, 267.
(7) Kresge, C. T.; Leonowicz, M. E.; Roth, W. J.; Vartuli, J. C. U.S. Patent, 5,098,684, 1992.
(8) Kresge, C. T.; Leonowicz, M. E.; Roth, W. J.; Vartuli, J. C.; Beck, J. S. *Nature* **1992**, *359*, 710.
(9) Beck, J. S.; Vartuli, J. C.; Roth, W. J.; Leonowicz, M. E.; Kresge, C. T.; Schmit, K. D.; Chu, C. T.-W.; Olson, D. H.; Sheppard, E. W.; McCullen, S. B.; Higgins, J. B.; Schlenker, J. L. *J. Am. Chem. Soc.* **1992**, *114*, 10 834.
(10) Armengol, E.; Cano, M. L.; Corma, A.; Garcia, H.; Navarro, M. T. *J. Chem. Soc., Chem. Commun.* **1995**, 519.
(11) Le, Q. N. U.S. Patent 5,191,134, 1993.
(12) Corma, A.; Navarro, M. T.; Perez-Pariente, J. *J. Chem. Soc., Chem. Commun.* **1994**, 147.
(13) Reddy, J. S.; Sayari A. *J. Chem. Soc., Chem. Commun.* **1995**, 2231.
(14) Reddy, J. S.; Dicko, A.; Sayari, A. In *Synthesis of Porous Materials: Zeolites, Clays and Nanostructures*; Occelli, M., and Kessler, H., Eds.; Marcel Dekker: New York, 1997; p 405.
(15) Gontier, S.; Tuel, A. *Stud. Surf. Sci. Catal.* **1997**, *105*, 1085.
(16) Reddy, K. M.; Moudrakovski, I.; Sayari, A.; *J. Chem. Soc. Chem., Commun.* **1994**, 1059.
(17) Das, T. K.; Chaudhari, K.; Chandwadkar, A. J.; Sivasanker, S. *J. Chem. Soc., Chem. Commun.* **1995**, 2495.
(18) Tuel, A.; Gontier, S.; Teissier, R. *J. Chem. Soc., Chem. Commun.* **1996**, 651.
(19) Gontier, S.; Tue, A. *Appl. Catal. A: General* **1996**, *143*, 125.

(20) Occelli, M. L.; Biz, S.; Aurox, A. *Appl. Catal. A: General* **1999**, *183*, 231.
(21) Barret, E. P.; Joyner, L. G.; Halenda, P. P. *J. Am. Chem. Soc*. **1951**, *73*, 373.
(22) Luan, Z.; Xu, J.; He, H.; Klinowski, J. *J. Phys. Chem*. **1996**, *100*, 19 595.
(23) Chang, Z.; Zhu, Z.; Kevan, L. *J. Phys. Chem., B* **1999**, *103*, 9442.
(24) Gregg, S. J.; Sing, K. S. W. *Adsorption, Surface Area and Porosity*; Academic Press Inc.: London, 1982; Chapter 4.
(25) Luan, Z.; He, H.; Zhou, W.; Cheng, C.-F.; Klinowski, J. *J. Chem. Soc., Faraday Trans*. **1995**, *91*, 2955.
(26) Boccuti, M. R.; Rao, K. M.; Zecchina, A.; Leofanti, G.; Petrini, G. *Stud. Surf. Sci. Catal*. **1989**, *48*, 133.
(27) Perego, G.; Bellussi, G.; Corno, C.; Taramasso, M.; Buonomo, F.; Esposito, A. *Stud. Surf. Sci. Catal*. **1986**, *28*, 129.
(28) Torralvo, M. J.; Alario, M. A. *J. Catal*. **1984**, *86*, 473.
(29) Liu, H.; Feng, L.; Zhang, X.; Xue, Q. *J. Phys. Chem.* **1995**, *99*, 332.
(30) Bobricheva, I. V.; Stavitsky, I. A.; Yermolaev, V. K.; Kotsarenko, V. P.; Shmachkova, V. P.; Kochubey, D. I. *Catal. Lett.* **1998**, *56*, 23.
(31) Prakash, A. M.; Kevan, L. *J. Catal.* **1998**, *978*, 586.
(32) Prakash, A. M.; Kevan, L.; Zahedi-Niaki, M. H.; Kaliaguine, S. *J. Phys. Chem.* **1999**, *103*, 831.
(33) Luan, Z.; Kevan, L. *J. Phys. Chem. B* **1997**, *101*, 2020.
(34) Goodman, B. A.; Raynor, J. B. In *Adv. Inorg. Chem. Radiochem.*; Emeleus, H. J., Sharpe, A. G., Eds.; Academic Press: New York, 1970, Vol. 13, p 135.
(35) Geobaldo, F.; Bordiga, S.; Zecchina, A.; Giamello, E.; Leofanti, G.; Petrini, G. *Catal. Lett.* **1992**, *16*, 109.
(36) Che, M.; Giamello, E. *Stud. Surf. Sci. Catal*. **1990**, *57B*, 265.
(37) Anpo, M.; Che, M.; Fubini, B.; Garrone, E.; Giamello, E.; Pagamini, M. C. *Topics Catal.* **1999**, *8*, 189.